processes

MDPI

Article

Research on the Application of Structural Topology Optimisation in the High-Precision Design of a Press Machine Frame

Zeqi Tong [1,2,*], Cheng Shen [3], Jie Fang [1,2], Mingming Ding [1] and Huimin Tao [1]

[1] Zhejiang Engineering Research Center of Advanced Water Conservancy Equipment, Zhejiang University of Water Resources and Electric Power, Hangzhou 310018, China; dingliumingming@163.com (M.D.); taohm@zjweu.edu.cn (H.T.)
[2] College of Mechanical and Electrical Engineering, China Jiliang University, Hangzhou 310018, China
[3] Electric Aviation R&D Center, Zhejiang Longchuang Motor Technology Innovation Co., Ltd., Shaoxing 312300, China; shencheng126@foxmail.com
* Correspondence: tongzq@zjweu.edu.cn

Abstract: This article aims to optimise the structure of a press machine to enhance its stability and accuracy, as well as reduce the frame deformation during processing. The outer supporting frame of the JH31-250 press machine (Zhejiang Weili Forging Machinery Co., Ltd, Shaoxing, China) is used as a typical sample for exploring optimisation. Commercial software is utilised to conduct a finite element analysis on the three-dimensional model of the press machine frame. A topological optimisation algorithm using the solid isotropic microstructures with penalisation (SIMP) method is then applied to improve the structure of the press frame. The size of the topological structure is further refined with the response surface method and particle swarm optimisation method to ensure it is more relevant to engineering application. The analysis results indicate that the initial frame's deformation under the static conditions is 0.4229 mm, and after optimisation, the deformed structural displacement is 0.2548 mm, a decrease of 39.75%. Additionally, a simplified experimental method is designed to effectively validate the simulation and the proposed design.

Keywords: press frame design; finite element analysis; topology optimisation; response surface method; stereo lithography appearance

Citation: Tong, Z.; Shen, C.; Fang, J.; Ding, M.; Tao, H. Research on the Application of Structural Topology Optimisation in the High-Precision Design of a Press Machine Frame. *Processes* **2024**, *12*, 226. https://doi.org/10.3390/pr12010226

Academic Editor: Raul D. S. G. Campilho

Received: 3 January 2024
Revised: 17 January 2024
Accepted: 18 January 2024
Published: 20 January 2024

1. Introduction

In the 21st century, the manufacturing industry places great value on forging machinery, which is essential for producing components by the plastic deformation of materials [1]. This process changes the external shapes or sizes of the materials and modifies their performances using external forces. As the workpieces and machine tools are tightly in contact with each other during the process, the reduced deformation and improved stiffness of machine tools have practical implications for manufacturing accuracy and product quality [2–4]. It is essential for forging equipment to be simple, reliable and of high stiffness to meet increasingly complex technological requirements. As a result, the high-precision design of press machines has become a focus of research internationally [5–7].

Mechanical structure design is the inverse problem of structural analysis. The press machine's final requirements are functional availability, quality stability, processability, and an extended service life. Under these conditions, the load capacity of kernel components, as well as their strength, stiffness, and operational accuracy, will be improved. Figure 1 illustrates the general design process for industrial products. If the performance of the conceptual configuration cannot be comprehensively evaluated, mechanical engineers may need to repeatedly modify and iterate over multiple stages. In practical mechanical engineering, which emphasises efficiency, it is difficult to obtain self-innovative configurations with improved performance. This article focuses on the effective design of conceptual configurations and associated technologies. Mechanical structure conceptual design involves

optimising a structure's topology, size, and shape. Topology optimisation involves optimising the layout and structure of materials by defining rules within a given design space. This concept can be traced back to Michell's truss design theory [8]. Schmit et al. [9] proposed size optimisation as a technique for optimising the various parameters of a structure, while Zienkiewicz and Campbell [10] first proposed shape optimisation for box structure design. Shape optimisation involves optimising the boundary or shape of a structure. Topology optimisation is an innovative technology used for structural optimisation. It employs a performance-driven forward design mode and is widely used in this field [11]. Topological optimisation is widely regarded as one of the most innovative and effective design methods [12,13].

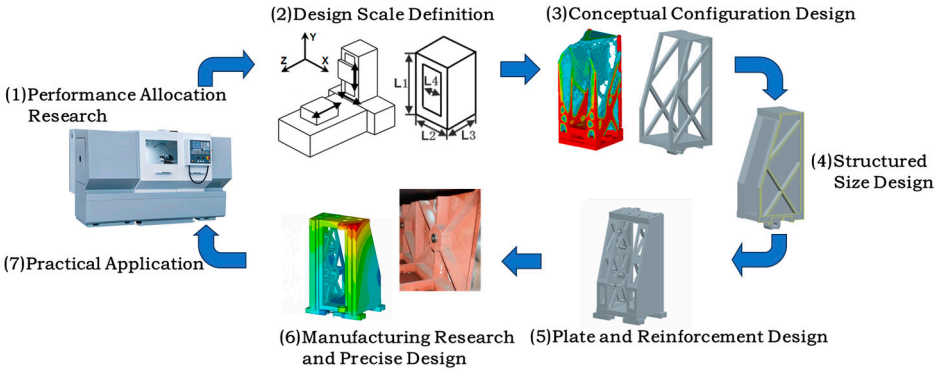

Figure 1. General design process for industrial products.

The topology optimisation method follows a performance-driven design scheme and can generate a structure with a reasonable material distribution, excellent performance conditions, and light-weight requirements. Ahmadi et al. [14] proposed a hierarchical construction method for optimising press performance. The method incorporates overhang constraints and support structure requirements into topology optimisation, making it suitable for high-resolution topology optimisation. Canelas et al. [15] proposed a precise quadratic topological expansion optimisation method based on a Kohn–Vogelius-like functional to solve the problem of anti-axisymmetric electromagnetic levitation. Guillen et al. [16] developed a framework for the topological optimisation of finned heat exchangers that combines fluid dynamic optimisation programmes to reduce the drop in pressure in the heat exchanger during operation. Lin [17] applied topological optimisation methods to facilitate the design of nonmanufacturable design features and ensure their reliability. Duan [18] used SIMP methods to conduct topological optimisation on a high-speed hydraulic press, achieving a structure with better quality and higher stiffness. Raz et al. [19] used different commercial optimisation tools (Tosca, Nastran, and Frustum) to create a new design of crossbeams for mechanical forging presses. Son et al. [20] proposed a design for a thermal forging machine structure based on impact control methods, optimising its transient dynamic stiffness. Yan et al. [21] proposed a buffer structure design for stamping machine tools to reduce the impact load on the dynamic and noise effects of the machine tools. In summary, structure optimisation methods offer theoretical guidance for structure design and are an efficient means of optimisation. However, because of the numerous internal components of a press, few studies have considered the concept of innovative structural topology design practically. Stereolithography apparatus photocurable plastics have excellent stiffness properties and are widely used for exploring and developing innovative structures for the quasi-static support of small deformation structures [22–24]. Therefore, we aimed to fully utilise the advantages of this technology to establish a closed-loop industrial design process that is more easily implementable for specific problems. This will expand the role of topology optimisation methods in the structural optimisation design of industrial equipment such as presses.

This article explores the use of structural topology optimisation in the high-precision design of press machine frames, as shown in Figure 2. In Section 2 of the article, the finite element analysis of the press frame based on the design scale definition is presented. In Section 3, topology optimisation is used to enhance the design of the support structures on both sides of the frame, resulting in a conceptual configuration design. In Section 4, to reduce the complexity caused by the topology model and numerical simplification, the manufacturing process is considered, and the size design with a plate and reinforcement is obtained. The response surface method and particle swarm optimisation method are employed to optimise the size of the simplified results. In Section 5, an experimental method based on stereolithography apparatus is designed to effectively validate the simulation and the proposed design. Considering the effective design of the conceptual configurations and associated technologies, a closed-loop industrial design process is more easily implementable for specific problems. The combination of the methods provides complementary benefits. The investigated design example reduces the deformation of the frame and improves its stiffness while ensuring an efficient manufacturing process.

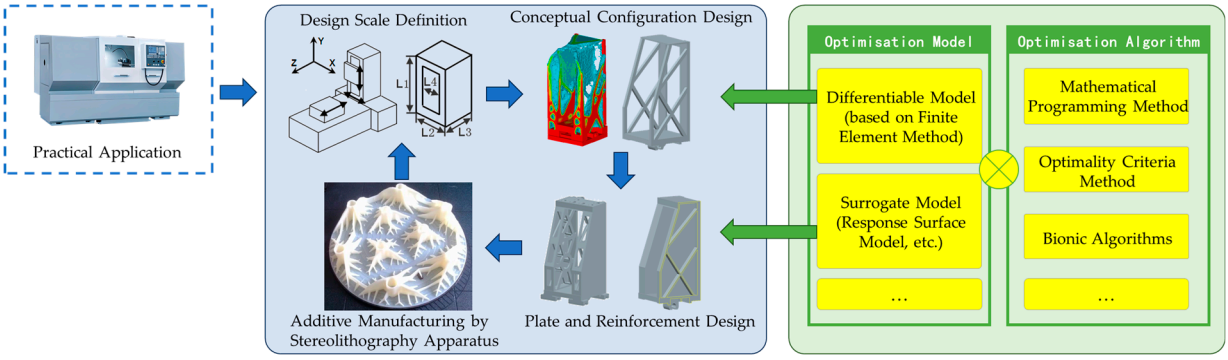

Figure 2. Closed-loop design process based on structural optimisation and additive manufacturing.

2. Finite Element Analysis

This article discusses the process of structural optimisation by an evaluation of the finite element numerical simulation's performance. The main objective of frame topological design is to find a reasonable overall structural stress transmission path, rather than focusing on local stress concentration. To achieve this, it is necessary to create a reasonable engineering structural mechanics model and simplify it according to the mechanical performance requirements of the press. We first analysed the structural form and working state of the JH31-250 press. Then, we used the Saint Venant principle to simplify details such as chamfers and bolts [25–27]. After, we performed the structural finite element simulation modelling and analysis.

2.1. Functional Overview of JH31-250 Press

This paper focused on the JH31-250 press [28], depicted in Figure 3a. This press frame has straight sidewalls that are easy to assemble, good vibration absorption, and is more suitable for mass production. The JH31-250 press comprises a frame, workbench, transmission structure, clutch, brake, and other components. The press operates by transforming the circular motion of the crankshaft into the vertical reciprocating motion of the ram through the slider–crank mechanism. The slide holds the upper die of the mould, whereas the worktable holds the lower die. The slide's upper and lower linear movements complete the mould's closing, forcefully pressing the workpiece to cause the plastic deformation or fracture of the metal material. This process enables the production and processing of parts. The press load in the forging process is a short-term impact load. The motor drives the flywheel to accelerate the rotation and store energy during idle periods. The flywheel decelerates during working periods to release energy and form the force required for forging.

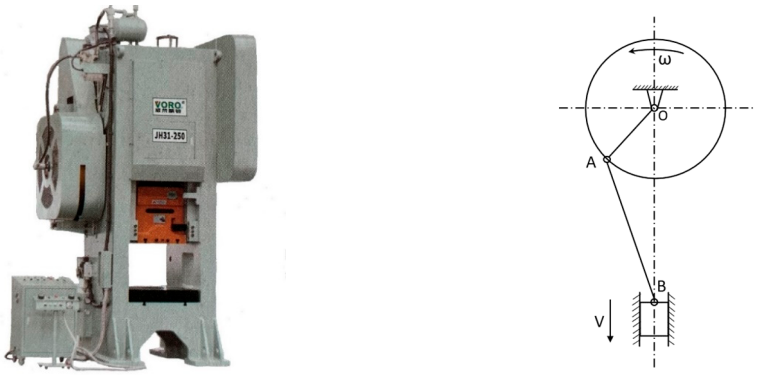

(**a**) (**b**)

Figure 3. The JH31-250 press: (**a**) image of the overall press object; (**b**) slider–crank mechanism of the press.

Figure 3b illustrates the slider–crank mechanism of the press, where point O denotes the centre of rotation, point A represents the connection between the press frame and the crankshaft, and point B represents the connection between the connecting rod and the slider. The radius of the crankshaft is denoted by OA, and the length of the connecting rod is denoted by AB. When the crankshaft rotates at an angular velocity of ω, the slider moves up and down in a straight line at a speed of v.

The sidewalls are the primary supporting components of the press and also the largest. Their mass accounts for over 60% of the entire machine. They support all the deformation force generated by the press in the working state and ensure the running accuracy of the slide, which are crucial to the performance of the entire machine. The press's optimal design necessitates a reasonable distribution of mass and structure in the press frame. This results in reduced deformation and displacement of the frame, as well as improved stiffness and working accuracy of the press.

2.2. Finite Element Modelling of JH31-250 Press

The JH31-250 press's main technical parameters were used to create a three-dimensional solid model of the frame. This model was then imported into finite element software to create a finite element model. The mechanical properties of the structure, including strength, stiffness, and natural frequency, were analysed after the boundary conditions were added and the mesh was divided. This analysis provides a reference for the subsequent structural optimisation design of the frame.

Because of the large size of the press frame, the reinforcement structure is mostly welded or bolted. Since these details have little influence on the overall strength and stiffness of the frame, they were ignored in the modelling of the real frame [17]. We smoothed the small round holes, filler holes, rounded corners, and chamfers, which do not have a significant influence on the structural performance; unnecessary raised parts, such as welds and small edge parts, were removed; threaded holes, rivet holes, oil holes, etc., were deleted. The simplified 3D solid model and the finite element model are shown in Figure 4.

The main support of the press consists of the frame and the workbench. The frame is welded with a Q235 steel plate and for the workbench with a QT500-7. Accordingly, the relevant materials were created in the software material library, and the material properties were defined for the numerical simulation. The specific material parameters are listed in Table 1.

(**a**) (**b**)

Figure 4. Modelling of the press frame: (**a**) three-dimensional solid model; (**b**) finite element model.

Table 1. Main material parameters of the press machine.

Part	Material	Poisson's Ratio	Young's Modulus/ MPa	Density/ Kg mm^{-3}	Yield Strength/ MPa
Frame	Q235	0.274	2.10×10^{-5}	7.83×10^{-9}	235
Workbench	QT500-7	0.293	1.62×10^{-5}	7.00×10^{-9}	320

The JH31-250 press frame is constructed entirely from thick plate material, so the three-dimensional solid element is used for the grid meshing of the discretising. As the aspect ratio of the wall thickness and the frame is very small, a flexible 10-node quadrilateral tetrahedral element was selected to improve the calculation accuracy. The mesh size was set to 50 mm. The mesh grid of the frame is shown in Figure 4b. After meshing, there were 90,633 elements and 169,521 nodes.

During operation, the press may experience frame deformation, which can impact the accuracy of the workpiece and potentially damage the die. To ensure robustness, the frame is designed to withstand a maximum nominal pressure of 2.5×10^6 N under worst working conditions. The surfaces supporting the crankshaft were coupled to two reference points (RP1 and RP2) separately, while the top surface of the workbench was coupled to RP3. The stiffness of the frame is defined as the ratio of the force to frame deformation.

(1) Displacement boundary condition

The press frame was fixed to the ground by bolts. To simulate the displacement of the frame, the base of the frame was constrained in the X-, Y-, and Z-axis directions, and its displacement was set to zero to prevent the rigid body motion of the press frame.

(2) Load boundary condition

Working loads were assigned at the crankshaft and the workbench, as a pair of interaction forces. According to the maximum nominal pressure, the working load had a magnitude of 1.25×10^3 kN and a positive direction along the *Y*-axis at the reference points (RP1 and RP2) of the two crankshaft holes. The force at the reference point (RP3) on the workbench was 2.5×10^3 kN, and the direction was negative direction along the *Y*-axis, as shown in Figure 5a. Considering the large mass of the frame, the effect of gravity could not be ignored. Therefore, the gravity load must be set, as shown in Figure 5b.

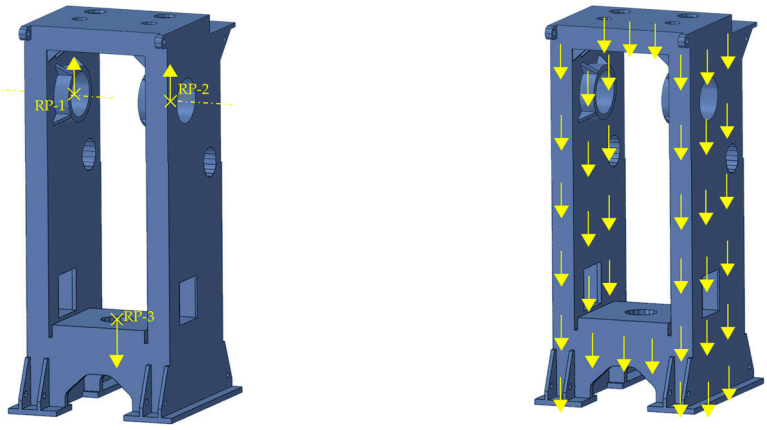

(**a**) (**b**)

Figure 5. The load on the press frame: (**a**) working load; (**b**) self-weight load.

2.3. Static Analysis of the Press Frame

On the basis of the established model and parameter settings, an overall static analysis of the press frame was conducted. The equivalent stress contour and the displacement contour of the press frame were obtained, as shown in Figure 6.

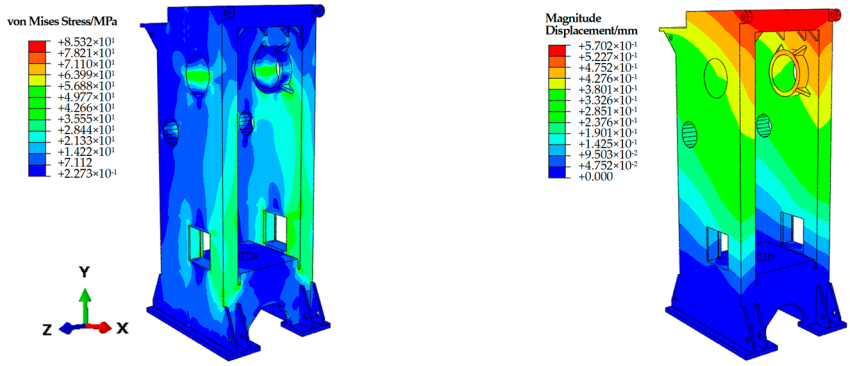

(**a**) (**b**)

Figure 6. Static analysis results on the initial frame: (**a**) stress contour; (**b**) displacement contour.

As can be seen from the figure, on the working load of the press, the stress distribution of the frame was symmetrical. There were concentrations of stress at the crankshaft support hole, inner plate of the frame, and front plate, and the maximum equivalent stress of the frame is 85.32 MPa. The square hole and the upper area of the frame were largely deformed, and the crankshaft support points had the largest magnitude displacement in the frame, with a maximum total displacement of 0.5702 mm, which had a great impact on the frame's stiffness.

Table 2 shows the maximum relative displacement of the space node RP1 corresponding to the crankshaft support hole and the centre node RP3 of the workbench surface, which was used as an indicator to measure the quantity of the relative deformation of the frame on the machining accuracy under working conditions. It is evident that the stress around the crankshaft support hole exceeded that of around the workbench. There was a slight difference in the magnitude of the deformation of the crankshaft support hole in three directions. The displacement in the *Y*-axis direction was larger than in the other directions due to the pressure direction of the slide block.

Table 2. Maximum relative displacement between RP1 and RP3 of the initial frame model.

Direction	Displacement of RP1/mm	Displacement of RP3/mm	Relative Displacement/mm
X-axis	-2.801×10^{-1}	-4.636×10^{-3}	
Y-axis	2.746×10^{-1}	-3.275×10^{-2}	4.249×10^{-1}
Z-axis	-1.010×10^{-1}	-2.255×10^{-5}	

To ensure the effectiveness and scalability of the method described in this article for industrial use, numerical simulation and optimisation iteration procedures are required to be time-saving. We input the analysis task into commercial software using a personal computer with a hardware environment of an Intel i7 10700 K and 32 GB RAM (without GPU acceleration), and the runtime cost was 3 min and 43 s. Therefore, this indicates that the simulation process is efficient and controllable.

3. Structural Topology Optimisation

The above analysis indicated that the press experiences deformation during operation, which impacts the stiffness of the frame, causes mould deformation, and, ultimately, affects the manufacturing accuracy of the workpieces. In order to meet the assembly requirements and ensure the machining accuracy, it is necessary to optimise the structure of the frame [29].

The topological optimisation method is based on the conception that the material distribution is variable, and the structural optimisation is solved by deleting the elements that have little influence on the structural stiffness. In this paper, the SIMP method [30–32] is used to find the optimal mass distribution in the conceptual design stage by planning the stress transmission path in the structure. By redistributing materials (described as pseudo-density) in the design space, the extremum structure topology that meets the design requirements can be obtained [33,34].

3.1. Mathematical Modelling of Maximum Structural Stiffness

In this example, the most appropriate index for stiffness evaluation is the ratio of the working load to the displacement between the workbench and the crankshaft support point. This can be written as the design objective function, which is the maximum $\varphi(\mathbf{X}) = \mathrm{F}/(\mathrm{u}_1 - \mathrm{u}_2)$. Given that the working load quantities at these two points are equal as the force and the reaction force, it can also be expressed as the minimum $f(\mathbf{X}) = [\mathrm{F}, -\mathrm{F}] \times [\mathrm{u}_1, \mathrm{u}_2]^{\mathrm{T}} = \mathbf{U}^{\mathrm{T}}\mathbf{K}\mathbf{U}$ (where column vector **F** denotes the applied external force, column vector **U** represents the deformation displacement, **K** is the stiffness matrix, and they are subjected to the finite element equation $\mathbf{F} = \mathbf{K}\mathbf{U}$). The latter expression is more commonly used in structural optimisation problems [35], because the finite element equation can be fully compatible with more complex load situations, since the working load is often not in the form of a point load when applied to the machine tools. Considering the multi-objective structural optimisation problem under multiple working load distributions on the worktable plane during normal operation of the machine tool, it is sufficient to specify the distribution form of the distributed force **F**. However, if the ratios of the different load conditions are inconsistent or the design objectives are not uniformly optimal, it is necessary to consider the corresponding multiple optimisation problems and draw the Pareto frontier to obtain more reasonable design results. Considering the stability of the forging station during operation, we will not discuss the details on this matter.

The design domain for topology optimisation includes the two replenished side walls. The column formulas for topology optimisation are as follows [36]:

$$\begin{cases} \text{find} \quad \mathbf{X} = [x_1, x_2, \cdots, x_n]^T \\ \min \quad f(\mathbf{X}) = \mathbf{F}^{\mathrm{T}}\mathbf{U} \\ \text{subject to} \begin{cases} V \le V^* \\ \mathbf{F} = \mathbf{K}\mathbf{U} \\ \mathbf{X}_i \in \{0,1\}\ i = 1,2,3,\cdots,n \end{cases} \end{cases} \tag{1}$$

where the design variable is the structure's pseudo-density represented by x, and n represents the number of elements. The objective of optimisation, $f(\mathbf{X})$, represents the compliance of the structure's frame, and it can be proved that minimum compliance means maximum global stiffness. In addition, V is the volume of the optimised structure, and V^* is the volume of the structure to be optimised. The constraint condition is set as the volume fraction to ensure that the optimised model's structural volume matches that of the model's before optimisation.

The interpolation expression of the elastic matrix is given as:

$$E(x_i) = E_{\min} + x_i^p \Delta E \quad i \in [1, n] \tag{2}$$

$$\mathbf{K} = \sum_{i=1}^{n} (E_{min} + x_i^p \Delta E)\mathbf{k}_i \tag{3}$$

The penalty factor, p, is used in this equation. The penalty factor can cause the design variable to tend toward 0 or 1. Additionally, the equation includes the elastic modulus of element i, $E(x_i)$; the elastic modulus of the excavated part, $E_{\min}$; the elastic modulus of the remaining entity, E_0; and $\Delta E = E_0 - E_{\min}$. The stiffness matrix, $\mathbf{K}$, and the stiffness matrix of the i-th element, $\mathbf{k}_i$, are also included. During the optimisation process, the structure's pseudo-density, x, is continuously updated. The final result is a material with a pseudo-density of 1, while any material with a pseudo-density of 0 is removed, resulting in the optimised structure.

The optimisation problem could be solved using several different approaches [37]. For conciseness, we demonstrate the flow of the standard optimality criteria (OC) method [38] to be used, as shown in Figure 7.

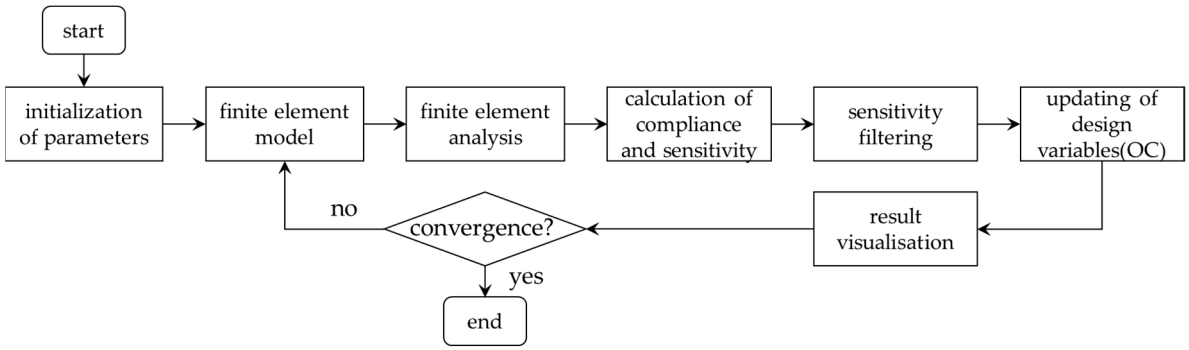

Figure 7. Flow of the structural topology optimisation for coding and numerical analysis.

3.2. Establishing the Design Domain for Optimising

The topology optimisation analysis of the frame was based on its static analysis. According to the selected frame design domain, the subsequent optimisation area of the frame was filled. Then, the frame structure optimisation model was established, and the material properties of each part of the frame were defined in the preprocessing module based on the material type of the static analysis. As the frame structure optimisation model has a relatively regular shape, a hexahedral structured grid was used to improve accuracy. This type of mesh is of good quality and creates smooth regions, with a boundary fitting that closely matches that of the actual model. It is suitable for calculating surface stress concentration and other related aspects [39]. Figure 8 shows that the filled, complete finite element frame model had a mesh size of 35 mm, with 63,001 mesh cells and 79,865 nodes.

As the topology optimisation of the press frame structure relies on the results of the static analysis, it is crucial that the contact and boundary conditions parameters used in the model before the optimisation are consistent with the parameters set in Section 2.

(**a**) (**b**)

Figure 8. Model for topology optimisation: (**a**) complete finite element model; (**b**) design domain.

3.3. Parameter Settings for Topology Optimisation

The aim of optimising the structure of a press body is to enhance its stiffness, strength, and other performance characteristics, as well as to ensure the press runs accurately during operation. After the finite element parameters are initialised in the optimal model with the numerical parameters, the optimisation process starts automatically, and the topological optimisation of the frame is carried out. The process of structural topology optimisation involves three main steps.

(1) Creating the optimisation tasks: Topological optimisation aims to maximise the utilisation rate of materials in the design domain, so the definition of the domains are crucial. For the purpose of structural optimisation, we identified the design domain of the support structure on both sides of the frame. The pseudo-density of the grid cells in the design domain was set as the design variable, with the minimum density set as 0.001, the maximum density set as 1, and the change amount of each design cycle set as 0.02. The topology optimisation design aims to achieve an element density distribution of roughly 0/1 by penalising intermediate density values. The penalty parameter's effectiveness improves as its p-value increases. However, if the p value is too large, matrix singularity may occur, leading to errors in the optimisation result. Therefore, the selected p-value is 3 [36].

(2) Assigning the objective function: The objective function was set as the minimum compliance (i.e., maximum global stiffness). The optimisation response was defined as the global variable under the volume constraint. The volume fraction before and after optimisation was set as the constraint condition, and it was set to 34.8%, which was the same as the volume ratio of the initial frame structure.

(3) Executing the optimisation tasks: Geometric constraints should be set to execute optimisation tasks on the frame design domain. To improve the accuracy of the optimisation, the non-optimized domain of the frame, excluding the design domain, should be created as a freezing domain. The optimisation process can then proceed to complete the task.

3.4. Optimal Structural Topology

The design domain of the structural frame was optimised, and the optimised conceptual topology configuration is shown in Figure 9. The iterative process converged after 60 steps, taking a total of approximately 3 h. The figure displays the material distribution (as pseudo-density) of the topologically optimised structure, which is similar to the stress transmission path inside the initial structural frame. Additionally, the figure presents the quantified distribution of materials. The inner panel area on both sides has a dense material distribution, indicating high force in this region. The supporting holes of the two sidewalls mainly retain material on the lower side, with a small amount distributed at the connecting points above the holes. The distribution of material on the vertical sides of the square hole is greater, and there are reinforcements on both the upper and lower sides.

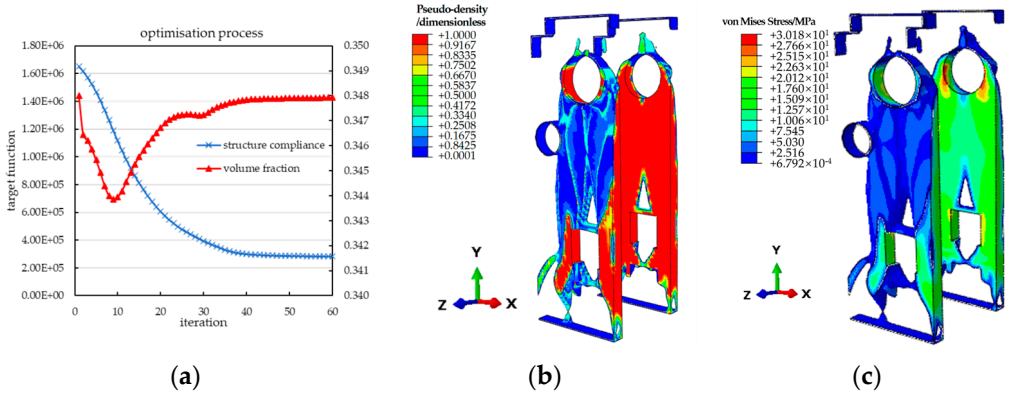

Figure 9. Display of the topologically optimised frame in the design domain: (**a**) iterations of the optimisation process; (**b**) pseudo-density contour; (**c**) von Mises stress contour.

Table 3 shows the relative deformation and displacement of the frame extracted from the optimised conceptual topology configuration. The table shows that the conceptual topology optimisation configuration of the structure's frame, when subjected to external load, experienced a 26.06% decrease in the relative displacement along the *Y*-axis direction compared to the initial model. Additionally, the overall relative deformation of the frame decreased to 0.2371 mm, which is a 44.20% decrease compared to the initial model.

Table 3. Maximum relative displacement between RP1 and RP3 of the topological optimised frame model.

Direction	Displacement of RP1/mm	Displacement of RP3/mm	Relative Displacement/mm
X-axis	4.152×10^{-3}	-1.583×10^{-2}	
Y-axis	-3.344×10^{-2}	1.933×10^{-1}	2.371×10^{-1}
Z-axis	1.158×10^{-4}	-6.627×10^{-2}	

It is also evident that the displacement of the support hole in the topology structure was smaller in all three directions when loaded compared to the structural static analysis of the initial frame model. Additionally, the overall topological structure of the experiences reduced these relative deformations and displacements, meeting the target requirement of increased frame stiffness.

4. Structural Size Optimisation Based on Optimal Topological Structure

The topological optimisation method is a conceptual design approach that optimises material distribution based on constraints, providing the designer with a rough conceptual layout. The optimisation results must then be reconstructed and the design domain regularised to clarify in detail the shape, position, direction, and size of the structure. This ensures that the structure is in line with engineering specifications and enhances the manufacturability. In structural size optimisation, ensuring the optimality for solutions is also important. However, the explicit relationship between structural size and performance is not obvious. Therefore, the response surface surrogate model method is used to approximate this mapping relationship. As the response surface function is a quantity-valued function with lower dimensions of input variables, solving its extremum points is relatively easy. Therefore, we used the efficient biomimetic algorithm of particle swarm to search the response surface briefly.

4.1. Regularity of the Topological Structure

For engineering applications, topology optimisation results may be too abstract to be processed using plate reinforcement materials. Therefore, it is necessary to regulate the topology configuration to meet engineering requirements. During this process, it is

important to consider the impact of the optimised design on maintenance, part replacement, and scalability, and to organise it reasonably. Given that the press frame is constructed from thick welded metal plates, we converted the topology configuration into a reinforced structure with a consistent reinforcement height. This facilitates the placement of metal skin on the outer side.

On the basis of the optimised conceptual topology configuration and the stress transmission path, the two side walls of the frame were reconstructed, as shown in Figure 10. Square plates were added to connect the crankshaft support holes and square holes in the inner area of the walls. The supporting reinforcements were positioned vertically at the high stress points on the two sides of the square hole. A connecting reinforcement was added to the upper end of the crankshaft support hole to connect the upper cover of the frame. The remaining external outline is welded with thin iron sheets.

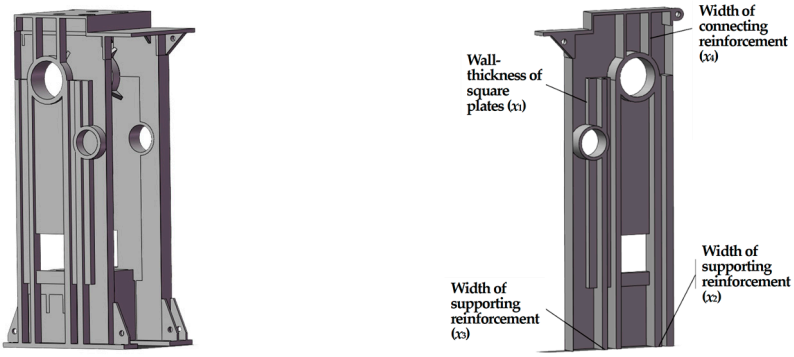

(**a**) (**b**)

Figure 10. Parametric model of the frame: (**a**) initial model for size optimisation; (**b**) design variables in design domain.

4.2. Response Surface Modelling

The response surface method (RSM) is a statistical technique used to determine the optimal combination of input parameters and to obtain the optimal system output. It involves establishing a mathematical model to represent the relationship between the system input and output. It involves establishing a mathematical model of the relationship between system input and output, which can be solved using simple polynomials with a small amount of experimental data. This makes it an easy-to-implement and -operate method for the optimal experimental design and analysis of complex systems. Compared to topology optimisation, stress transmission path material distribution is directly determined through response surface design and particle swarm optimisation. This approach is more suitable for optimising structure shape and size according to actual manufacturing requirements.

Figure 10b shows the parameterised geometric dimensions of the structured reinforced slab. The design variables of the frame include the thickness of the inner square plate (x_1), the width of the right reinforcement of the square hole (x_2), the width of the left reinforcement of the square hole (x_3), and the width of the connecting reinforcement at the upper end of the support hole (x_4). The output variable of the response surface design is selected as the maximum relative deformation displacement between the points RP1 and RP3 in the frame.

The response surface method requires constructing a target approximation function using partially determined experimental sample data [40]. To quickly and effectively select sample points, the DoE experimental design can be employed. The experimental design utilises the central composite design (CCD) method [41], which involves additional levels in the experimental process. This approach enhances prediction accuracy and improves efficiency.

When designing the CCD experiment, it is important to consider the number of independent variables. The number of experimental samples required can be calculated

using the formula $M = 2^n + 2n + 1$, where n is the number of independent variables. To ensure a reasonable quadratic polynomial fitting, the number of samples, M, must be greater than $N = (n + 1)(n + 2)/2$. For the size optimisation problem in this paper, the design variables are x_1, x_2, x_3, and x_4. Considering the volume constraint, one of the variables is passive, so $n = 3$, resulting in $M = 15$ and $N = 10$, satisfying $M > N$. The following numerical discussion shows that it is sufficient in this case. Otherwise, an alternative design method for the experiment would be adopted. Please refer to Table 4 for the range of experimental design variables.

Table 4. Ranges of design variables.

Parameter	Minimum Value/mm	Maximum Value/mm
x_2	70	100
x_3	45	75
x_4	30	60

The reinforcement structure must connect the cover plate reinforcement and the crankshaft support hole reinforcement. Therefore, the width of the upper end of the x_4 support hole reinforcement must be greater than or equal to 30 mm. The study employed the central composite experiment method to design the experimental variables. The corresponding structure frame model was reconstructed with 3D modelling software using different experimental parameters. The model was then imported into finite element software for numerical simulation, which yielded the relative deformation and displacement of the frame under different parameters. The numerical simulation results are presented in Table 5.

Table 5. Parameter values of central composite design and numerical simulation results of the frame.

CCD No.	Design Variables				Relative Displacement
	x_1/mm (Passive)	x_2/mm	x_3/mm	x_4/mm	U/mm
1	86.71	59.02	60.00	45.00	0.263052
2	86.39	70.00	45.00	60.00	0.256535
3	72.38	100.00	45.00	30.00	0.264296
4	50.79	110.98	60.00	45.00	0.270708
5	67.52	100.00	45.00	60.00	0.268385
6	66.29	85.00	60.00	70.98	0.255213
7	90.75	70.00	45.00	30.00	0.255638
8	73.48	70.00	75.00	30.00	0.261181
9	85.98	85.00	34.02	45.00	0.265501
10	68.67	70.00	75.00	60.00	0.262959
11	74.68	85.00	60.00	19.02	0.251085
12	70.59	85.00	60.00	45.00	0.253207
13	50.70	100.00	75.00	30.00	0.256296
14	51.95	85.00	85.98	45.00	0.260777
15	45.27	100.00	75.00	60.00	0.260738

The objective function of the press's body size optimisation is transformed into a quadratic polynomial using the response surface method, making it easy to solve. The variables are fitted with the target parameters using the polynomial least squares method. This shows that the quadratic polynomial fits well, and the resulting polynomial is shown in Formula (4). The error analysis of the response surface fitting results indicates an R^2 value of 0.9904, demonstrating a good fitting. Figure 11 displays the response surface.

$$\begin{aligned} U \quad &= 10^{-5} \times (37379 - 249.9x_2 - 51.84x_3 - 19.96x_4 + 2x_2^2 \\ &+1.45x_3^2 - 0.0341x_4^2 - 1.5341x_2x_3 + 0.3253x_2x_4 + 0.0686x_3x_4) \end{aligned} \tag{4}$$

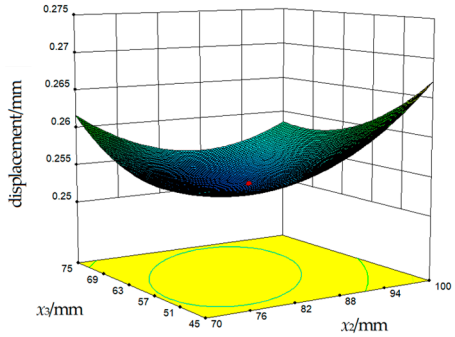

Figure 11. Slice of the response surface in 3 dimensions (x_1 and x_4 are fixed).

The optimisation problem is formulated as shown:

$$\begin{cases} \text{find} & \mathbf{X} = [x_1, x_2, x_3, x_4]^{\mathrm{T}} \\ \min & U = U(\mathbf{X}) \\ \text{subject to} & V(\mathbf{X}) \leq V^* \end{cases} \tag{5}$$

Because of the low dimensionality of the independent variable, obtaining a slice of the response surface is easy. Nongradient algorithms, such as biomimetic algorithms (e.g., particle swarm optimisation algorithm, PSO), can quickly provide numerical solutions for this optimisation problem.

4.3. Response Surface Model Searching by PSO

The corresponding minimisation problem posed by the response surface equation is a typical unconstrained nonconvex optimisation problem, which can be solved using many mature numerical methods. In this case, the particle swarm optimisation algorithm is used to solve the problem. Throughout the iteration process of the algorithm, optimal particle information is transmitted to other particles via a particle speed to facilitate information sharing and ultimately find the optimal solution to the problem. This method offers several benefits, including strong memory, fast search rates, and good convergence. The variable parameters are dynamically optimised using quadratic polynomials with response surface visualisation.

The particle swarm optimisation algorithm utilises the concepts of 'swarm' and 'evolution'. It employs bulk and mass-free particles that fly at a certain speed in the search space to find the global optimal solution based on flight experience and swarm flight. The evolution equation's expression is also used [42]:

$$V_{ij}(n+1) = \omega V_{ij}(n) + c_1 r_{1j}\left[P_{ij} - x_{ij}(n)\right] + c_2 r_{2j}\left[P_{gj} - x_{ij}(n)\right] \tag{6}$$

$$x_{ij}(n+1) = x_{ij}(n) + V_{ij}(n+1) \tag{7}$$

The variables used in this study were as follows: i represents the particle label, j represents the particle dimension, n represents evolutional generation, V_{ij} represents particle velocity, and ω represents weight. The space position of the particle is denoted by x_{ij}, whereas P_{ij} and P_{gj} represent the optimal coordinates of individual particles and particle space, respectively. Additionally, c_1 and c_2 are learning factors, and r_{1j} and r_{2j} are random numbers between 0 and 1.

The response surface polynomial (4) was used as the objective function, and the particle swarm optimisation algorithm was employed to solve the optimisation problem. The optimal solution was x^* = [76.27, 81.95, 57.91, 30.38], and the minimum value of the maximum relative displacement of the frame was 0.25204 mm. The variable value of x^*, corresponding to the optimal solution obtained by the response surface and particle swarm optimisation algorithm, was used for parametric modelling. Commercial FEM software was used to conduct a static structural analysis on the three-dimensional model. The

resulting diagrams in Figure 12 show the equivalent stress cloud and overall displacement of the optimised frame structure. The cloud image shows that the maximum equivalent stress of the optimised frame structure decreased to 82.09 MPa, and the overall maximum displacement of the frame decreased to 0.2672 mm, which is an improvement compared to the initial press frame structure.

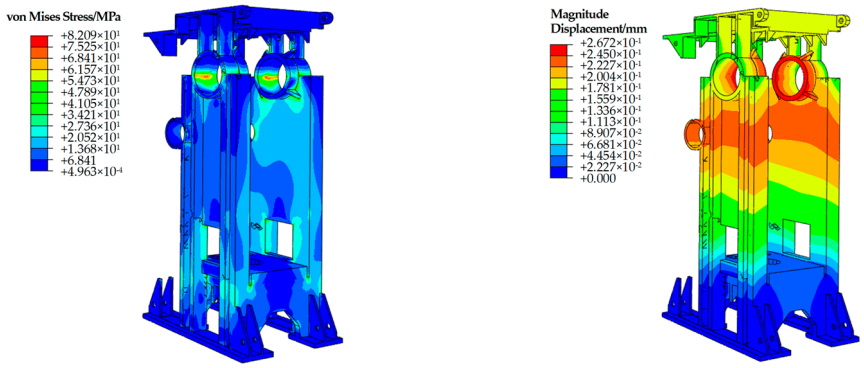

(**a**) (**b**)

Figure 12. Static analysis results for the optimised frame: (**a**) stress contour; (**b**) displacement contour.

Table 6 shows the maximum relative displacement between the crankshaft support hole of the press body and the surface of the workbench after optimisation under working conditions, which was extracted from the output of the postprocessing task of the finite element analysis results. The optimisation results demonstrate a 40.03% decrease in the maximum relative displacement of the frame compared to the initial frame.

Table 6. Maximum relative displacement between RP1 and RP3 of the particle-swarm-optimised frame model.

Direction	Displacement of RP1/mm	Displacement of RP3/mm	Relative Displacement/mm
X-axis	-1.557×10^{-3}	-2.224×10^{-3}	
Y-axis	2.018×10^{-1}	-3.582×10^{-2}	2.548×10^{-1}
Z-axis	-9.197×10^{-2}	1.460×10^{-5}	

By comparing the maximum relative displacement of the frame obtained by particle swarm optimisation with the finite element analysis data, it is evident that the difference between the two values is 1.1%. This finding confirms the reliability of the response surface design combined with particle swarm optimisation.

The optimised frame model underwent a modal analysis, and the results are presented in Table 7. Considering the frequency of the external excitation source, it is evident that the low-order natural frequency of the frame is much higher than that of the excitation source, thus preventing resonance.

Table 7. Natural frequency of the particle-swarm-optimised frame model.

Order	1	2	3	4	5
Frequency/Hz	19.631	51.325	55.999	85.043	104.98

5. Experimental Validation

By analysing the static structure of the press frame, it is possible to obtain the stress distribution, overall displacement, and relative deformation displacement of the initial structure. On the basis of the analysis results, the design structure area of the frame is determined, and the static structure of the design area is optimised using the topology

optimisation method to obtain the optimal frame structure. To confirm the superiority of the design scheme, this paper utilised an electronic universal testing machine to construct a test bench for the structure frame experiments. The finite element analysis results were converted into 3D printing models as test parts, from which the mechanical property advantages of the press frame design scheme was verified.

5.1. Experiment on the 8228 Resin Standard Specimen

Stereo lithography appearance (SLA) is a technology that utilises the monomer in the photocuring polymer material. The monomer molecules are induced to polymerise the liquid photocuring material by light, usually ultraviolet light, resulting in the formation of a polymer material [43]. After years of development, SLA is currently the only rapid prototyping technology capable of printing large-scale models, which provides unique advantages [44].

The resin material sample is displayed in Figure 13. The mechanical properties of the product were altered, to some extent, because of the differences in 3D printing methods among manufacturers. To enhance the accuracy of the body model simulation, we conducted a unidirectional tensile test on the 8228 resin sample. The sample was 100 mm in length and 18 mm in width, with varied thicknesses of 1.5 mm, 2 mm, and 2.5 mm. We obtained the actual mechanical property parameters from the test.

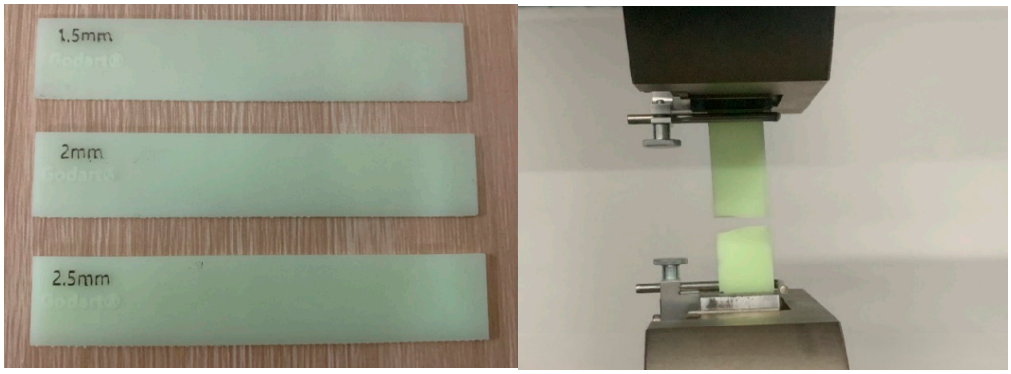

Figure 13. The 8228 resin specimens' tensile test.

The 34TM-kN electronic universal material testing machine was chosen as the tensile test equipment. It had a maximum load capacity of 50 kN and a tensile speed of 2.5 mm/min. Figure 14 shows the tensile stress–strain curve of the sample, and Table 8 displays the performance parameters of the 8228 resin.

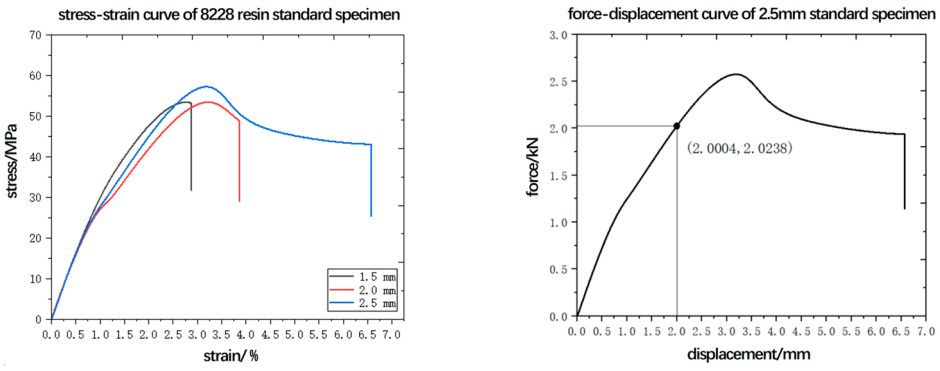

(**a**) (**b**)

Figure 14. Tensile curves of the 8228 resin specimens: (**a**) stress-strain curves of 8228 resin standard specimens; (**b**) force-displacement curve of 2.5mm standard specimen.

Table 8. Material performance characteristics of the 8228 resin specimens.

Material	Young's Modulus/MPa	Yield Strength /MPa	Poisson's Ratio	Density /Kg mm^{-3}
8228 resin	1378	50–58	0.3	1.15×10^{-6}

During the formation of liquid materials, certain phenomena such as uneven internal filling and defects may occur. However, as shown in Figure 14, the slopes of the specimens with varying thicknesses were consistent during the elastic stage. This paper selected the material parameters of the elastic stage for numerical simulation to study the stiffness of the frame structure under normal working conditions. This lays the foundation for subsequent numerical simulations of the frame model.

5.2. Simulation of the 8228 Resin Standard Specimen

To ensure the reliability of the finite element simulation, we established a sample model using the finite element software and conducted a tensile test, as depicted in Figure 15.

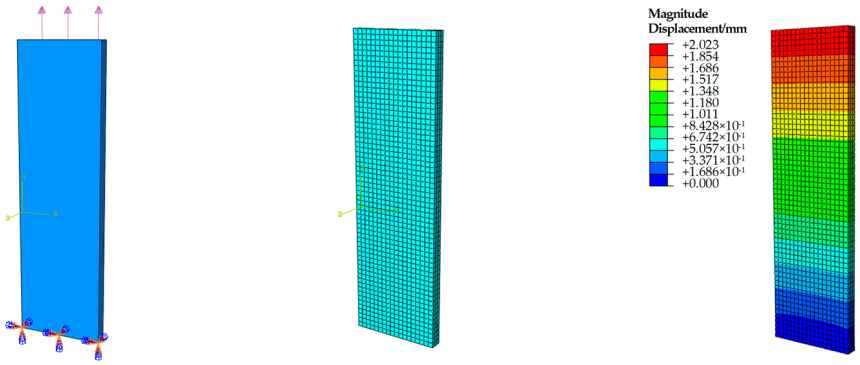

(**a**) (**b**) (**c**)

Figure 15. Numerical simulation of the 8228 specimens: (**a**) boundary conditions of load and displacement; (**b**) finite element model; (**c**) deformation result with static analysis.

The following specific operations were carried out:

1. Establishment of a finite element model: The sample used in the tensile experiment had the geometric parameters of a 100 mm length, 18 mm width, and 2.5 mm thickness. The distance between the upper and lower ends of the sample held by the fixture during the tensile exercise was 20 mm. Therefore, the model's length during the numerical simulation was set to 60 mm.
2. Material parameter setting: the material parameters of the finite element model of the sample were set using the data in Table 8.
3. Model discretising and grid meshing: The model was divided using a structured grid with a grid size of 1 mm. The resulting model consisted of 3348 units and 4788 nodes.
4. Load and displacement boundary condition setting: on the basis of the tensile test, the model was fixed with zero degrees of freedom in the three directions at the bottom and subjected to a surface load of 2 kN at the upper end.

Figure 15c shows that the sample model deformed by 2.023 mm under a tensile force of 2 kN, which is consistent with the solid sample's tensile result. This indicates that the material properties of 8228 were correctly set and the finite element simulation's results are effective.

5.3. Experiment on the 8228 Resin's Optimised Model

The SLA technology was utilised to reduce the frame models of the two presses by 1/10 at the same scale. The 8828 high-strength resin material was used, and the same

printing parameters were set to print out the resin model of the structure before and after optimisation. The performances of the frame model structure before and after optimisation were observed by a force analysis of the two solid models. The specific model is shown in Figure 16a. The frame model on the left is pre-optimised, while the one on the right is optimised.

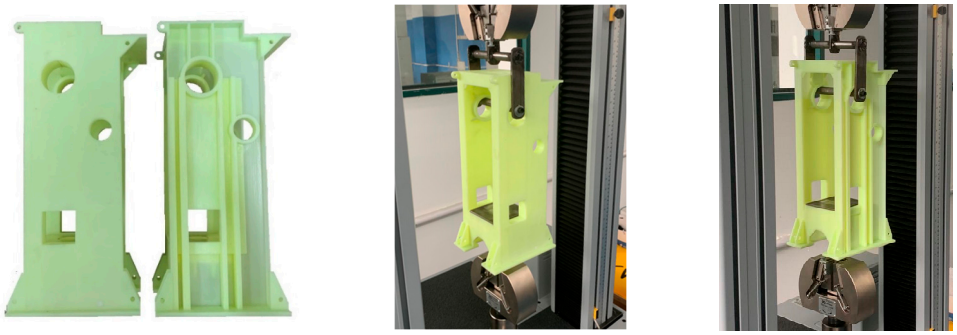

(**a**) (**b**) (**c**)

Figure 16. Quasi-static experiment of resin frame model: (**a**) solid, resin frame model by SLA; (**b**) initial structure; (**c**) optimised structure.

To assess the performances of the optimised frame structure's model and the initial frame model, tensile experiments were conducted on both models before and after optimisation. The experiments were carried out using a universal electronic testing machine with the same load direction setting as the simulation. Please refer to Figure 16b,c for the specific clamping mode and tensile direction.

The electronic universal testing machine was set to a tensile speed of 0.5 mm/min. Forces were applied to both frame models, and their corresponding deformations were recorded in real time using sensors. The resulting curves for the forces and deformations are shown in Figure 17.

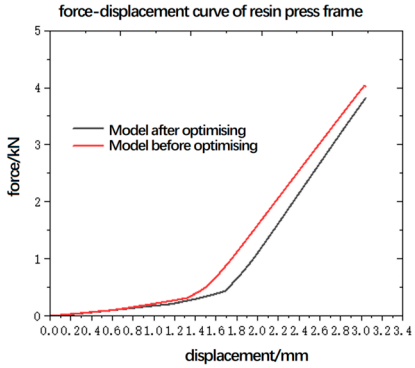

Figure 17. Tensile test force–displacement elastoplastic curves of the resin press frame.

By comparing the curves, it is evident that the frame is in an untensed state before the pulling force reaches 0.5 kN. When the pulling force exceeds 0.5 kN, the frame deforms and displaces gradually with the increase in the pulling force. In this tensed section, the stiffness of the structure can be determined by calculating the slope of the deformation and displacement curves in the linear elastic stage. The results demonstrate that the optimised frame model experiences less deformation and displacement than the pre-optimised frame model when subjected to the same tension. This provides evidence that the frame structure optimisation scheme is correct and did, indeed, improve the frame stiffness. Specifically, at a 3 kN force, the optimised model deformed by 1.145 mm, whereas the pre-optimised model deformed by 1.299 mm.

5.4. Simulation of the 8228 Resin's Optimised Model

For the analytical simulation of the optimised press frame model of the resin, the following specific operations were performed:

1. Establishment of a finite element model: the initial frame model and the statically optimised frame model were reduced by 1/10 and imported into commercial software.
2. Material parameter setting: the relevant materials were established based on the material performance parameters obtained from the specimen tensile test, and the material parameters of the frame model were set accordingly.
3. Model discretising and grid meshing: The initial and optimised frame models were divided using a tetrahedral mesh. The mesh size was set to 5 mm. The initial frame model consisted of 103,287 elements and 184,779 nodes, whereas the optimised model had 90,906 units and 169,717 nodes. The initial frame model consisted of 103,287 elements and 184,779 nodes, whereas the optimised model had 90,906 units and 169,717 nodes.
4. Load and displacement boundary conditions setting: The load and boundary conditions were set for the simulated solid-frame experiment, with a 1500 N force applied at the characteristic points of the two crankshaft support holes. The boundary conditions were also established. To achieve complete constraints, the freedom of movement in all three directions of the workbench area was set to zero.

A static structural analysis was conducted on the resin frame model before and after static optimisation. The resulting cloud map of frame stress and deformation is shown in Figure 18.

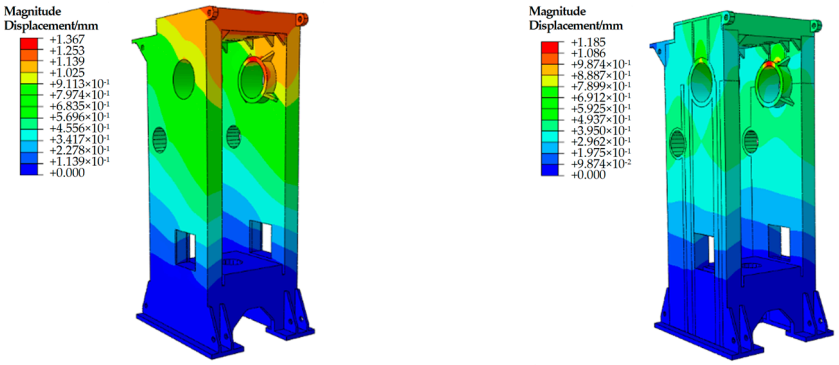

(**a**) (**b**)

Figure 18. Static analysis of the resin frame model: (**a**) deformation contour before optimisation; (**b**) deformation contour after optimisation.

The analysis of the initial resin model's static structure shows that the overall deformation of the frame was U = 1.367 mm, which differs by 4.97% from the experimental result. The optimised resin model's static analysis shows that the overall deformation of the frame was U = 1.185 mm, which differs by 3.38% from the experiment. The validity of the finite element simulation results for the frame can be verified by considering the experimental and calculation errors comprehensively.

6. Discussion

During the press's operation, the majority of the force is borne by the frame, resulting in deformation. The displacement of the frame crankshaft support hole relative to the workbench can cause damage to the mould and even affect the accuracy of the product. Therefore, the evaluation standard for the frame load deformation was based on the relative displacement between the space node of the support hole and the centre node of the workbench RP3. To ensure the reliability of the press frame optimisation scheme with

real materials, we compared the simulation results of the 8228 resin frame model with those of the initial Q235 material.

The initial frame model's relative displacement by static analysis is shown in Table 9. It can be compared with the relative displacement of the 8228 resin frame model in Table 10.

Table 9. Maximum relative displacement between RP1 and RP3 of the initial frame model of resin.

Direction	Displacement of RP1/mm	Displacement of RP3/mm	Relative Displacement/mm
X-axis	-4.950×10^{-1}	-7.985×10^{-3}	
Y-axis	5.055×10^{-1}	-5.507×10^{-2}	7.631×10^{-1}
Z-axis	-1.770×10^{-1}	-3.934×10^{-5}	

Table 10. Maximum relative displacement between RP1 and RP3 of the size-optimised frame model of resin.

Direction	Displacement of RP1/mm	Displacement of RP3/mm	Relative Displacement/mm
X-axis	1.480×10^{-3}	-3.935×10^{-3}	
Y-axis	3.701×10^{-1}	-5.839×10^{-2}	4.563×10^{-1}
Z-axis	-1.569×10^{-1}	-4.909×10^{-7}	

Comparing the data in Tables 9 and 10, it is evident that the load-relative deformation of the initial frame model was 0.7631 mm, whereas the optimised load-relative deformation of the frame model was 0.4563 mm. This indicates a decrease of 40.2% in the relative deformation and displacement of the frame, with a difference of $\Delta = 0.3068$ mm.

The numerical simulation analysis results of the sample model are consistent with the tensile experimental data, verifying the correctness of the material parameters of 8228 and the effectiveness of the finite element simulation. Because the static analysis results for the resin frame model were shown to be substantially consistent with the experimental results for the solid resin frame, we can conclude that the numerical simulation method is reliable and the static structure optimisation scheme of the frame under the resin material is effective.

At the same time, the static optimisation of the 8228 resin frame resulted in a 40.2% decrease in the maximum relative displacement of the fuselage. The results in Section 4.3 demonstrate a 40.03% decrease in the maximum relative displacement of the Q235 frame after static optimisation. The difference between the pre- and postoptimisation values is only 0.17%, indicating the feasibility of the static structure optimisation scheme using real materials. These findings suggest that the airframe dynamic optimisation scheme using real materials is also reliable. Table 6 shows the relative displacement obtained by static analysis of the frame model after the optimisation outlined in Section 4.3, which was then compared with the relative displacement of the initial frame model, as shown in Table 2 in Section 2.3.

Upon comparing the data in the two tables, it is evident that the load-relative deformation of the initial frame model was 0.4249 mm, whereas the optimised load-relative deformation of the fuselage model was 0.2548 mm. This indicates a difference of 0.1701 mm in the relative deformation and displacement of the frame, resulting in a decrease of 40.03%.

The results are consolidated in Figure 19. It can be seen that the displacement results for the optimised frame models are superior to the initial model for both the resin and steel models. The initial model exhibits symmetry in the z-direction, resulting in minimal displacement in that direction. However, there is a significant displacement in the *x*-axis direction (i.e., the front and rear directions of the machine) in addition to the larger displacement of the body in the working load direction. The optimised structure achieved a good balance by arranging materials in a reasonable manner along the *x*-axis. This is also

a crucial factor in structural optimisation. Therefore, it can be concluded that the optimised frame structure has greater static stiffness and meets the structural design requirements.

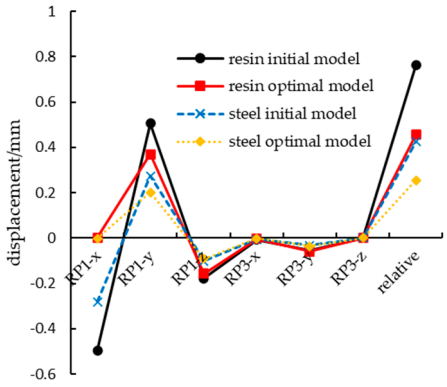

Figure 19. Analytical comparison of the frame models made of resin/steel and before/after optimisation.

The experimental scheme described in this article is suitable for verifying the design of static load-bearing structures. Although it provides preliminary support for simulation and optimisation design, it is still recommended to conduct more extensive physical testing to further verify the new design under actual load conditions. The simulation results suggest that appropriate dynamic displacement sensors [45] (or indirectly derived from velocity/acceleration sensors) can be chosen to measure the workbench deformation. Laser interferometers can also be used for position accuracy detection [46,47]. Additionally, to establish an accurate dynamic model of a pressure machine tool, it is necessary to measure physical parameters such as mass moment of inertia, stiffness, and damping at key positions of the system [48,49]. The implementation of an online state monitoring and analysis system involves the use of various sensors, such as vibration sensors, swing sensors, pressure sensors, pressure pulsation sensors, and speed sensors. The online vibration monitoring instrument is a crucial tool for dynamic performance testing. It can trigger synchronous parallel sampling across all channels.

7. Conclusions

Maintaining the high stiffness performance of the machine tool structure under different working conditions is crucial for the structural design of the press. A stable and reliable forging machine tool with high stiffness is an essential component of the construction of an intelligent precision forging production line. This paper analysed and studied the JH31-250 forging press, which is the core piece of equipment on the production line, to improve its structural stiffness and accuracy under working conditions. It also explores the optimal design method of the press frame structure under specific working conditions. The main conclusions are as follows:

(1) A simplified experimental verification method was proposed to verify the accuracy of the finite element simulation of the press. The material sample and solid model of the body before and after static optimisation were printed using light curing technology. A static analysis was conducted to obtain the material characteristics of the 8228 resin material. The reliability of the material parameters was verified by comparing them with the simulation results. Secondly, a tensile test and static structural analysis were conducted on the resin frame and finite element model, respectively. The numerical analysis results were then compared with the solid test results to verify the validity of the numerical simulation. Finally, the correctness and effectiveness of the frame structure optimisation scheme for metal materials was verified by comparing it with the results for optimising frame structures made of resin materials.

(2) This paper establishes a three-dimensional model of the frame based on the main technical parameters of the JH31-250 press. The frame structure was then numerically simulated and analysed in combination with the stress characteristics. On the basis of

the analysis of the static structure, the primary stress of the frame was concentrated in the support hole, the inner plate of the frame, and the front plate area. The frame's maximum equivalent stress was 85.32 MPa, while the overall maximum displacement and relative displacement were 0.5702 mm and 0.4249 mm, respectively. This demonstrates the usefulness of the method beyond its current application. The optimisation method presented in this article has potential applications in improving other machine tools and mechanical structures.

(3) This paper employed a topological optimisation method to statically optimise the support structure area on both sides of the frame. The optimisation objective function was set as the minimum compliance, with the volume fraction serving as the constraint condition. A mathematical model for topological optimisation was established to perform conceptual optimisation in the design domain of the frame. The regularised frame reinforcement structure's geometric size was used as the optimisation parameter, and the maximum relative displacement of the frame was the optimisation objective for the size optimisation based on the optimised conceptual configuration. After optimisation, the frame's maximum relative displacement was 0.2548 mm, resulting in a 40.03% decrease in deformation compared to the initial model. Additionally, the static stiffness of the frame significantly improved.

Furthermore, this paper solely analysed and optimised the press frame structure from a static perspective. Future studies should aim to comprehensively consider both the static and dynamic structures and how to effectively combine them for overall structural optimisation. Because of the limited experimental conditions, the solid resin model of the optimised press body was established before and after the use of light-curing SLA technology on the press body. This model may have certain errors compared to the real metal material model. When conditions permit, conducting a real model experiment can further improve the analysis accuracy. This work provides a reference for designing high-stiffness structures for similar forging equipment.

Author Contributions: Conceptualisation, M.D.; methodology, Z.T.; software, Z.T. and C.S.; validation, H.T.; formal analysis, C.S.; data curation, J.F.; writing—original draft preparation, C.S.; writing—review and editing, M.D.; visualisation, C.S.; supervision, Z.T.; funding acquisition, M.D. All authors have read and agreed to the published version of the manuscript.

Funding: This research was funded by the Project of Fundamental Commonweal Research of Zhejiang Province (grant no. LGG22E050034) and "Pioneer" and "Leading Goose" R&D Program of Zhejiang (grant no. 2022C01070).

Data Availability Statement: The data used to support the findings of this study are available from the corresponding author upon request.

Conflicts of Interest: Author Cheng Shen was employed by the company Zhejiang Longchuang Motor Technology Innovation Co., Ltd. The remaining authors declare that the research was conducted in the absence of any commercial or financial relationships that could be construed as a potential conflict of interest.

References

1. Fengque, P.; Yifei, T.; Fei, H.; Dongbo, L. Research on design of the smart factory for forging enterprise in the industry 4.0 environment. *Mechanika* **2017**, *23*, 146–152. [CrossRef]
2. Yutian, W.; Dong, W.; Zhang, S.; Zihan, T.; Liping, W.; Yanmin, L. Design and development of a five-axis machine tool with high accuracy, stiffness and efficiency for aero-engine casing manufacturing. *Chin. J. Aeronaut.* **2022**, *35*, 485–496.
3. Shi, Y.; Zhao, X.; Zhang, H.; Nie, Y.; Zhang, D. A new top-down design method for the stiffness of precision machine tools. *Int. J. Adv. Manuf. Technol.* **2016**, *83*, 1887–1904. [CrossRef]
4. Huang, D.T.-Y.; Lee, J.-J. On obtaining machine tool stiffness by CAE techniques. *Int. J. Mach. Tools Manuf.* **2001**, *41*, 1149–1163. [CrossRef]
5. Zhou, H.; Dong, P.; Zhao, S.; Geng, M.; Guo, Y.; Wang, Y. Interrupted plate porous media design for ionic liquid-type liquid piston hydrogen compressor and analysis of the effect on compression efficiency. *J. Energy Storage* **2022**, *51*, 104410. [CrossRef]
6. Li, C.; Qin, G.; Wang, H.; Geng, P. Constitutive modeling and dynamic recrystallization mechanism elaboration of FGH96 with severe hot deformation. *J. Mater. Res. Technol.* **2022**, *21*, 2947–2964. [CrossRef]

7. Mahmoudi, M.; Aboutalebi, M.; Salehi, M.; Moshaver, H.; Ebrahimi, G.; Vafaeenezhad, H. Microstructure evolution, hot deformation behaviour and processing map of Inconel X-750 superalloy in sub-solvus and super-solvus temperature ranges. *J. Mater. Res. Technol.* **2023**, *26*, 5594–5616. [CrossRef]
8. Maxwell, J. On Reciprocal Figures, Frames, and Diagrams of Force. *Trans. R. Soc. Edinb.* **1872**, *26*, 1–40. [CrossRef]
9. Schmit, L.A. Structural design by systematic synthesis. In Proceedings of the Second National Conference on Electronic Computation ASCE, Pittsburgh, PA, USA, 8–9 September 1960.
10. Francavilla, A.; Ramakrishnan, A.C.; Zienkiewicz, O. Optimization of shape to minimize stress concentration. *J. Strain Anal.* **1975**, *10*, 63–70. [CrossRef]
11. Eschenauer, H.A.; Olhoff, N. Topology optimization of continuum structures: A review. *Appl. Mech. Rev.* **2001**, *54*, 331–390. [CrossRef]
12. Ibhadode, O.; Zhang, Z.; Sixt, J.; Nsiempba, K.M.; Orakwe, J.; Martinez-Marchese, A.; Ero, O.; Shahabad, S.I.; Bonakdar, A.; Toyserkani, E. Topology optimization for metal additive manufacturing: Current trends, challenges, and future outlook. *Virtual Phys. Prototyp.* **2023**, *18*, e2181192. [CrossRef]
13. Li, Y.; Gao, T.; Zhou, Q.; Chen, P.; Yin, D.; Zhang, W. Layout design of thin-walled structures with lattices and stiffeners using multi-material topology optimization. *Chin. J. Aeronaut.* **2023**, *36*, 496–509. [CrossRef]
14. Hosseini Imeni, S.Z.; Kaabinejadian, A.; Ami Ahmadi, H.; Moghimi, M. Optimal design and sensitivity analysis of airfoil-shaped rotor blade for Savonius wind turbine by using response surface methodology. *Wind. Eng.* **2022**, *46*, 1203–1223. [CrossRef]
15. Canelas, A.; Roche, J.R. Shape and topology optimal design problems in electromagnetic casting. *Eng. Comput.* **2021**, *39*, 147–171. [CrossRef]
16. Guillen, D.P.; Abboud, A.W.; Bennink, J. Topology optimization of an airfoil fin microchannel heat exchanger using artificial intelligence. *Nucl. Eng. Des.* **2022**, *391*, 111737. [CrossRef]
17. Zhao, X.; Liu, Y.; Hua, L.; Mao, H. Finite element analysis and topology optimization of a 12000KN fine blanking press frame. *Struct. Multidiscip. Optim.* **2016**, *54*, 375–389. [CrossRef]
18. Duan, Z.D.; Wu, J.J. Topological optimization of frame of high speed hydraulic press based on generalized finite element modules. *Appl. Mech. Mater.* **2011**, *44*, 1828–1832. [CrossRef]
19. Raz, K.; Cechura, M. Usage of topological optimization in design of mechanical forging presses. *MM Sci. J.* **2018**, *11*, 2581–2584. [CrossRef]
20. Son, L.; Nakatani, D.; Matsuhisa, H.; Utsuno, H. Application of momentum exchange impact dampers to forging machine. *J. Syst. Des. Dyn.* **2008**, *2*, 1027–1039. [CrossRef]
21. Yan, X.; Chen, B. Energy-Efficiency Improvement and Processing Performance Optimization of Forging Hydraulic Presses Based on an Energy-Saving Buffer System. *Appl. Sci.* **2020**, *10*, 6020. [CrossRef]
22. Bartolo, P.; Kruth, J.-P.; Silva, J.; Levy, G.; Malshe, A.; Rajurkar, K.; Mitsuishi, M.; Ciurana, J.; Leu, M. Biomedical production of implants by additive electro-chemical and physical processes. *CIRP Ann.-Manuf. Technol.* **2012**, *61*, 635–655. [CrossRef]
23. Petrovic, V.; Vicente Haro Gonzalez, J.; Jorda Ferrando, O.; Delgado Gordillo, J.; Ramon Blasco Puchades, J.; Portoles Grinan, L. Additive layered manufacturing: Sectors of industrial application shown through case studies. *Int. J. Prod. Res.* **2011**, *49*, 1061–1079. [CrossRef]
24. Yanping, L.; Panding, W.; Jie, G.; Jikai, L.; Quhao, L.; Changmeng, L.; Xiaofan, H.; Liang, G.; Hao, L.; Hongshuai, L. Fundamental mechanics problems in metal additive manufacturing: A state-of-art review. *Adv. Mech.* **2021**, *51*, 648–701.
25. Xu, S.; Deng, X. An evaluation of simplified finite element models for spot-welded joints. *Finite Elem. Anal. Des.* **2004**, *40*, 1175–1194. [CrossRef]
26. D'Aniello, M.; Cassiano, D.; Landolfo, R. Simplified criteria for finite element modelling of European preloadable bolts. *Steel Compos. Struct* **2017**, *24*, 643–658.
27. Chan, T.-C.; Ullah, A.; Roy, B.; Chang, S.-L. Finite element analysis and structure optimization of a gantry-type high-precision machine tool. *Sci. Rep.* **2023**, *13*, 13006. [CrossRef]
28. Shen, C.; Ding, M.; Tong, Z.; Liu, J.; Zhang, C. Optimization design of the load-bearing structure of press frame based on minimum flexibility. In Proceedings of the Sixth International Conference on Intelligent Computing, Communication, and Devices (ICCD 2023), Hong Kong, China, 3–5 March 2023; pp. 333–343.
29. Ji, X.; Liao, S.; Zhang, X.; Gao, X.; Ma, R. Finite element analysis and optimization design of beam structure of forging press. *J. Phys. Conf. Ser.* **2021**, *1983*, 012018. [CrossRef]
30. Rozvany, G.I.; Zhou, M.; Birker, T. Generalized shape optimization without homogenization. *Struct. Optim.* **1992**, *4*, 250–252. [CrossRef]
31. Cazacu, R.; Grama, L. Overview of structural topology optimization methods for plane and solid structures. *Ann. Univ. Oradea Fascicle Manag. Technol. Eng.* **2014**, *23*, 1583–1591.
32. Challis, V.; Roberts, A.; Wilkins, A. Design of three dimensional isotropic microstructures for maximized stiffness and conductivity. *Int. J. Solids Struct.* **2008**, *45*, 4130–4146. [CrossRef]
33. Zuo, K.; Chen, L.; Zhang, Y.; Yang, J. Manufacturing-and machining-based topology optimization. *Int. J. Adv. Manuf. Technol.* **2006**, *27*, 531–536. [CrossRef]
34. Cheng, D.; Lu, X.; Sun, X. Multi-objective topology optimization of column structure for vertical machining center. *Procedia CIRP* **2018**, *78*, 279–284. [CrossRef]

35. Bendsoe, M.P.; Sigmund, O. *Topology Optimization: Theory, Methods, and Applications*; Springer Science & Business Media: Berlin/Heidelberg, Germany, 2003.
36. Sigmund, O. A 99 line topology optimization code written in Matlab. *Struct. Multidiscip. Optim.* **2001**, *21*, 120–127. [CrossRef]
37. Adby, P. *Introduction to Optimization Methods*; Springer Science & Business Media: Berlin/Heidelberg, Germany, 2013.
38. Prager, W.; Marcal, P.V. *Optimality Criteria in Structural Design*; Air Force Systems Command; Air Force Flight Dynamics Laboratory: Dayton, OH, USA, 1971.
39. Kim, J.W.; Lee, D.J. Characteristic interface conditions for multiblock high-order computation on singular structured grid. *AIAA J.* **2003**, *41*, 2341–2348. [CrossRef]
40. Liu, S.; Tong, Z.; Tang, Z.; Zhang, Z. Design optimization of the S-frame to improve crashworthiness. *Acta Mech. Sin.* **2014**, *30*, 589–599. [CrossRef]
41. Kleijnen, J.P. Design of experiments: Overview. In Proceedings of the 2008 Winter Simulation Conference, Miami, FL, USA, 7–10 December 2008; pp. 479–488.
42. Wang, D.; Tan, D.; Liu, L. Particle swarm optimization algorithm: An overview. *Soft Comput.* **2018**, *22*, 387–408. [CrossRef]
43. Huang, J.; Qin, Q.; Wang, J. A review of stereolithography: Processes and systems. *Processes* **2020**, *8*, 1138. [CrossRef]
44. Quan, H.; Zhang, T.; Xu, H.; Luo, S.; Nie, J.; Zhu, X. Photo-curing 3D printing technique and its challenges. *Bioact. Mater.* **2020**, *5*, 110–115. [CrossRef]
45. Mi, L.; Yin, G.-F.; Sun, M.-N.; Wang, X.-H. Effects of preloads on joints on dynamic stiffness of a whole machine tool structure. *J. Mech. Sci. Technol.* **2012**, *26*, 495–508. [CrossRef]
46. Kono, D.; Nishio, S.; Yamaji, I.; Matsubara, A. A method for stiffness tuning of machine tool supports considering contact stiffness. *Int. J. Mach. Tools Manuf.* **2015**, *90*, 50–59. [CrossRef]
47. Laspas, T.; Theissen, N.; Archenti, A. Novel methodology for the measurement and identification for quasi-static stiffness of five-axis machine tools. *Precis. Eng.* **2020**, *65*, 164–170. [CrossRef]
48. Gao, X.; Zhang, Y.; Zhang, H.; Wu, Q. Effects of machine tool configuration on its dynamics based on orthogonal experiment method. *Chin. J. Aeronaut.* **2012**, *25*, 285–291. [CrossRef]
49. Law, M.; Rentzsch, H.; Ihlenfeldt, S. Predicting mobile machine tool dynamics by experimental dynamic substructuring. *Int. J. Mach. Tools Manuf.* **2016**, *108*, 127–134. [CrossRef]